COMSOL
CONFERENCE
2023 MUNICH

3D Numerical Simulation of Resistance Sintering Process for Electrical Contact Applications for Breakers.

J. AMOVIN-ASSAGBA[1], V. BRUYERE[2], P. NAMY[2], C. DURAND[1], S. ROURE[1]

[1] SCHNEIDER ELECTRIC, 31 Rue Pierre Mendes France, EYBENS-FRANCE
[2] SIMTEC, 5 Rue Felix Poulat, GRENOBLE-France

Abstract

In circuit breakers, short-circuit breaking involves extreme conditions linked to the presence of an intense electric arc. This requires the use of specific electrical contacts consisting of a contact tip made of composite materials, assembled on a metallic substrate. SCHNEIDER ELECTRIC uses the resistance sintering technique for the sintering-assembly of silver-based composite electrical contact materials on copper substrates. It is a fast-sintering technique that combines heat generated by an electrical current and pressure to densify powder metallurgy parts. A variety of properties are required for the electrical tips (High electrical and thermal conductivity, good welding resistance, good densification state...). To control the resulting geometry as well as the final states of the sintering process, a 3D electro-thermo-mechanical model has been developed using COMSOL Multiphysics. Thanks to accurate knowledge of material properties and contact resistances, this numerical model is a predictive tool of these different final states, which can lead to better product quality. In our paper, we will describe the 3D model, the numerical modeling strategy and present also some obtained results.

Keywords: Sintering, Viscoelasticity, Thermal Balance, COMSOL Multiphysics

Introduction

SCHNEIDER ELECTRIC uses powder metallurgy combined with resistance sintering to produce electrical contacts by simultaneously sintering and bonding a cold compacted silver-based part to its support by Joule heating. Several silver-based composite materials such as AgC, AgWC or AgNi are used to achieve both good thermal and electrical conductivity and mechanical strength [1]. The powder mixing composition, the particle size and the final shape of the tips are crucial to guarantee the optimized properties [2,3] as well as the densification rate. As these properties strongly depend on the resistance sintering-assembly process conditions, it is important to efficiently control them through numerical simulation. At this stage, the sintering part is investigated. The model requires good knowledge of material properties. A Norton-Green law is used to describe the mechanical behavior of the tip [4]. Creep and sintering tests have been achieved on a Gleeble machine to define specific laws for the contact material to be implemented in the model. The heating is driven by the contact resistances (both electrical and thermal) especially between the tip and the electrode on one hand and the tip and the substrate on the other hand. Mikic model [5] is used to model the contact resistances at these interfaces.

In this paper, we will describe the 3D numerical model, and results obtained on a study case. Comparisons are made with experimental measurements and show that efficient knowledge of material properties and contact resistances lead to a very predictive model.

Numerical modeling

Geometry and operating conditions

The 3D geometry is shown in Figure 1 and is composed of different parts: the electrode (beige) and its holder (black) the tip (gray), the substrate (orange) and the cooling bar (red). Due to confidential reasons, the full description of the parts and their properties are not provided.

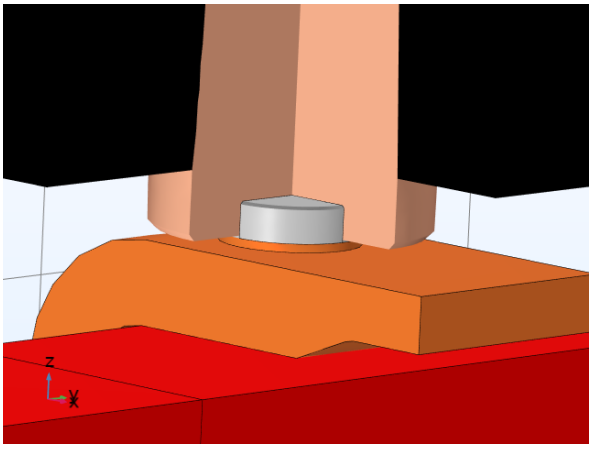

Figure 1: 3D geometry composed by an electrode (beige) and its holder (black), a tip (gray), a contact (orange), and the cooling bar (red). [Non-contractual design]

To densify the tip and attach it on its support, a current and a load are applied on the top of the electrode holder (Figure 2). A current phase and a holding phase are observed.

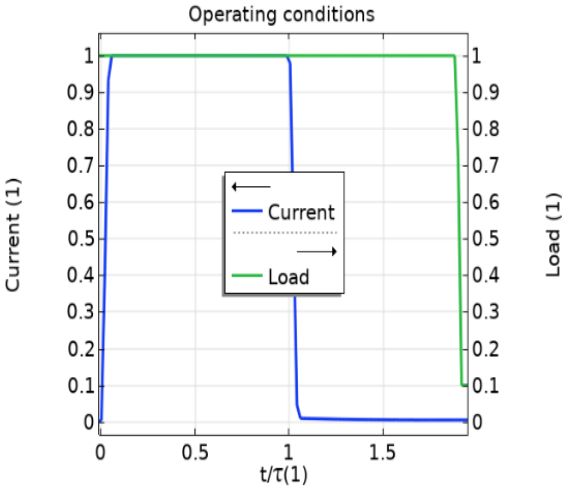

Figure 2: Operating conditions: Current (blue) and load (green).

Equations and boundary conditions

Three different "physics" (mechanical, electrical, and thermal) are involved in this process. The couplings between different physics are also considered. A brief description is done below.

Electrical problem

To estimate the electrical potential and current in each element, the current conservation law (Eq. 1) is solved.

$$\nabla \cdot (\sigma_{elec} \nabla V) = 0 \qquad \textit{Eq. 1}$$

where V is the electric potential and σ is the electrical conductivity of the material.

The electric field E_{elec} is defined by $E_{elec} = -\nabla V$ and is a resultant of the imposed current density $d_j = \sigma_{elec} \boldsymbol{E_{elec}} = -\sigma_{elec} \boldsymbol{\nabla} V$.

Thermal problem

Eq. 2 for heat transfer is solved, with $Q_{vol} = \sigma_{elec} (\nabla V)^2$ corresponding to the Joule heating (power) source term generated by the electric current flow through the material.

$$\boldsymbol{\rho Cp \frac{\partial T}{\partial t} = \nabla \cdot (\lambda \nabla T) + Q_{vol}} \qquad \textbf{\textit{Eq. 2}}$$

To consider the cooling in the bar, we compute an internal forced convective heat flux at cooling surfaces with Eq. 3:

$$\Phi_{th} = h \times (T - T_{ext}) \cdot S$$

$$h = \frac{\lambda}{D} f(Re, Pr) = \frac{\lambda}{D} Nu \qquad \textit{Eq. 3}$$

with λ the thermal conductivity, Re the Reynolds number, Pr the Prandtl number; Nu the Nusselt number, S the cooling surface and h the heat transfer coefficient.

This approach allows to compromise between imposing a cooling temperature and computing the Fluid Mechanics. It is representative of the industrial process as it considers the flow, hole diameter, and fluid nature.

An additional EDO is also solved to evaluate the maximum temperature at each node to consider the irreversibility aspect of the contact resistance evolution with the temperature.

Mechanical problem

To solve this problem by considering it mainly elastic (outside the tip), we need to find a displacement field $u_i\,(x,t)$ and a stress field $\sigma_{ij}\,(x,t)$ verifying the equations of motion (Eq. 4).

$$\sigma_{ij,j} + f_i = \rho \frac{\partial^2 u_i}{\partial t^2} \qquad \textit{Eq. 4}$$

For irreversible deformation of the tip, the viscoplastic Norton model associated with Green's criterion was chosen to model resistive sintering and is well-described in [6].

The contacts considered in the model are those of the tip (top, side, bottom), and the contact between the cooling bar and the contact. The penalty algorithm is used, and a sensitivity study was performed to ensure non-dependency. Comparisons are also made with other algorithms (especially Augmented Lagrangian method) to set a reasonable penalty factor.

Contact resistances

Contact resistances (CR) quantify the effects of thermal barriers (for thermal contact resistance TCR) and electrical barriers (for electrical contact resistance ECR) at the contact surfaces between two materials. This barrier is mainly due to the different nature of the materials and the imperfections at surface level.

The Mikic model [5], is used to evaluate the CR across every parts. This approach evaluates the CR in function of the contact pressure p, the local roughness, and the material properties as shown in Eq. 5. The roughness profile is described by the Root Mean Square (RMS) of the surface roughness height (σ_{asp}) and surface roughness slope (m_{asp}).

$$\frac{1}{TCR} = h_c^{therm} = 1.54 \cdot k_c \frac{m_{asp}}{\sigma_{asp}} \left(\frac{p\sqrt{2}}{m_{asp} E_c} \right)^{0.94}$$

$$\frac{1}{ECR} = h_c^{elec} = 1.54 \cdot \sigma_c \frac{m_{asp}}{\sigma_{asp}} \left(\frac{p\sqrt{2}}{m_{asp} E_c} \right)^{0.94} \qquad \textit{Eq. 5}$$

with k_c, the equivalent thermal conductivity $\frac{2}{k_c} = \frac{1}{k_1} + \frac{1}{k_2}$, $\frac{2}{\sigma_c} = \frac{1}{\sigma_1} + \frac{1}{\sigma_2}$, the equivalent electrical conductivity; E_c, the equivalent elastic modulus $\frac{1}{E_c} = \frac{1-\nu_1^2}{E_1} + \frac{1-\nu_2^2}{E_2}$, with E_i the Young modulus and ν_i the Poisson's ratio of each material i in contact.

More precise description and the use in the simulation of resistance sintering process was done in previous paper [7].

Numerical strategy and validations

Mesh

The mesh is composed of about 210.000 elements and is strongly defined by a refinement at contact boundaries to ensure a good computation of CR and of the penalty contact method. A sensitivity study about the mesh properties has also been performed to ensure no-dependency of the solution on the mesh.

Solvers

The BDF algorithm is selected as the time-dependent solver by carefully tuning the time-step and by using the "previous solution" feature to evaluate the temperature history. A segregated approach is adopted to solve this problem "block by block", and thus increase the time step and increase the saving in calculation time. The damping factor is set for each segregated step to ensure the numerical convergence under robust conditions.

The CPU time is roughly 11 hours with a PC of 8 processors and 128 Go RAM for the entire cycle.

Numerical validation

To numerically validate the approach, numerical balances are performed (results in *Figure 3*). The electrical power generated in the top of the electrode holder is plotted in blue.

$$P_{elec} = \iint_S (\boldsymbol{dj} \cdot \boldsymbol{n}) V \cdot dS \qquad \textit{Eq. 6}$$

The electrical resistances, encountered by the current flow from the top to the bottom, generate a resulting power. The thermal power is computed, both in volume source terms and surface source terms.

$$P_{Joule}^{Volume} = \iiint_{Volume} Q_{vol} \cdot dV$$

$$P_{Joule}^{Surface} = \iint_{Surf} Q_{surf} \cdot dS \qquad \textit{Eq. 7}$$

The thermal power generated is dissipated through cooling (Eq. 8), radiative losses (Eq. 9), and by body-to-body heat transfer (Eq. 10).

$$P_{th}^{cooling} = \iint_S h \times (T - T_{ext}) \cdot dS \qquad \textit{Eq. 8}$$

$$P_{Joule}^{Surface} = \iint_{S_{ambiant}} \varepsilon\sigma(T^4 - T_{amb}^4) \cdot dS \qquad \textit{Eq. 9}$$

$$P_{th}^{\Delta T} = \iiint_V \rho \cdot C_p \cdot \frac{\partial T}{\partial t} \cdot dV \qquad \textit{Eq. 10}$$

The first balance compares the generated power to the resulted thermal power (in both volume and surface terms). The second one compares the generated thermal power, to the dissipated thermal power. And as shown in Figure 3, power is well balanced, thus validating the numerical approach.

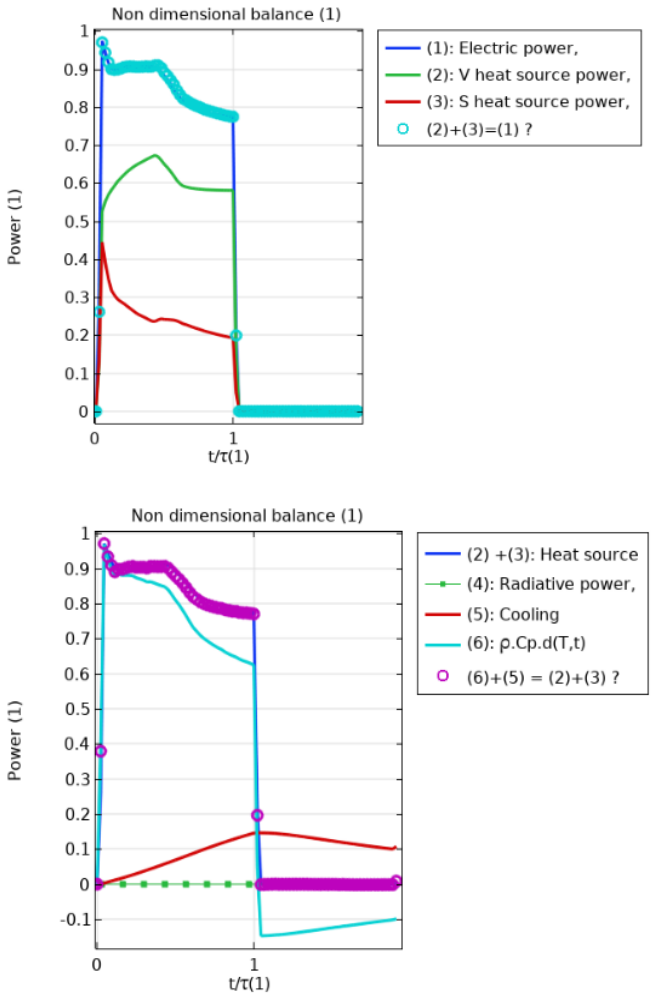

Figure 3: Power balances

Results and discussions

A study-case with a non-contractual geometry (for confidential reasons) is performed here with a duration of the applied current density of τ. The results presented here (except the comparisons) are ones of the study case.

The Figure 4 shows the non-dimensional electrical potential at different times and the potential gap between each interface. The electrical potential follows the power balance tendency

with a peak at $\tau/20$ which corresponds to the end of the current rise.

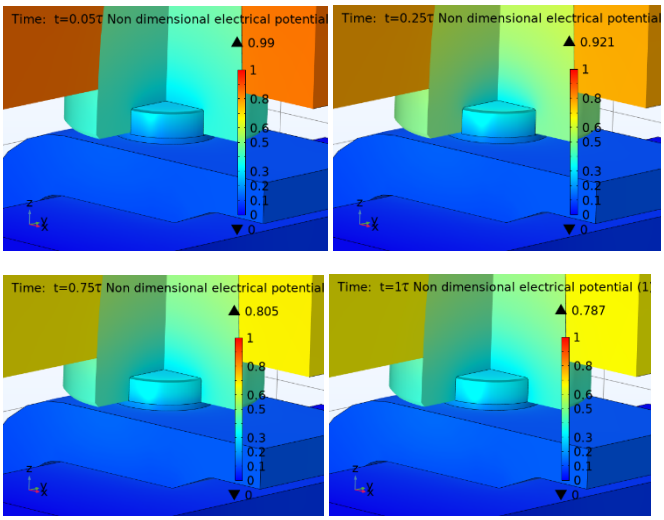

Figure 4 : Non dimensional electrical potential

The Figure 5 shows the non-dimensional temperature in every part (heat camera pallet) and the non-dimensional density of the tip (rainbow pallet) at different times.

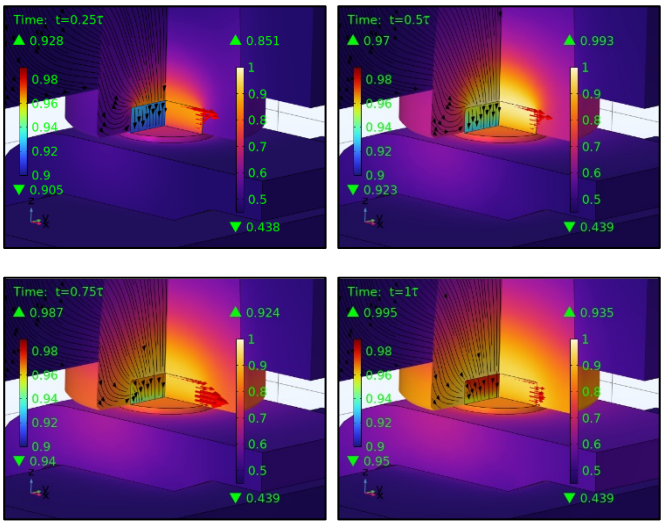

Figure 5: Non dimensional temperature (heat camera pallet) and tip's non dimensional density (Rainbow pallet). Black streamlines: current density; red arrows: Total heat flux in x direction.

For the temperature, we can see a general rise until $\tau/2$, a decrease then until $3\tau/4$ and finally a rise until τ. The decrease during the current phase is due to the contact between the side face of the electrode and the tip. As the tip is hotter than the side face of the electrode, an equilibrium phase occurs before a last temperature rise phase. The total heat flux arrows also emphasize this phenomenon showing lateral contact zones where heat is generated.

The density evolution is also shown and a densification from the top to the bottom is observed (Figure 5). Heterogeneities are also observed, due to the heterogeneities in the stress distribution in the tip (Figure 6). The more the tip is densified, the less important is the local stress.

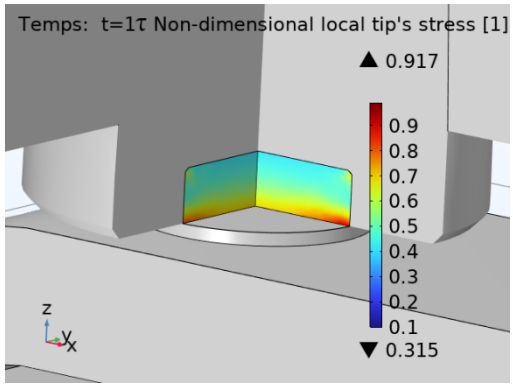

Figure 6: Non dimensional local stress at $t = \tau$.

The Figure 7 shows the Nusselt number on the heated surfaces in the bar at $t = \tau$ (Eq. 11 of Dittus-Boetler). The closer we are to the heating area, the bigger is the Nusselt number. The order of magnitude corresponds to ones obtained in the literature ([8]) for internal forced convective heat flux.

$$Nu = 0.023 \times Re^{4/5} \times Pr^{0.4} \qquad Eq.\ 11$$

The black isovalue, shows that the most heated area tends to have a wall temperature above $2 \cdot T_0$, with T_0 the initial temperature. The magenta isovalue make it possible to evaluate the distance to the welding point where the wall temperature is less than $T_0 + 5$.

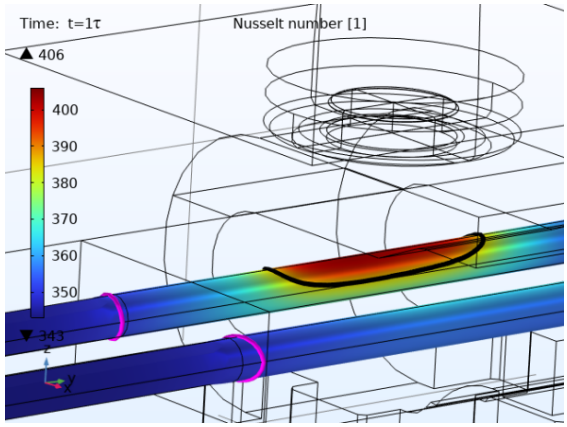

Figure 7: Nusselt number on the cooling surfaces / Magenta isovalue: $T < T_0 + 5$, and black isovalue for: $T > 2 \cdot T_0$; with T_0, the initial temperature

Nevertheless, a more precise computation must be made as the geometry is irregular and the local velocity is not computed.

Comparison with experimental measurements

In this part, we present comparisons with experimental measurement on real contact (different from the study case geometry) to validate the numerical model. The tooling elements are the same except their geometries.

The Figure 8 shows the non-dimensional temperature of a point located in the electrode. The numerical result (in blue) is confronted to experimental measures (markers). Very good approvals are obtained with the order of magnitude as well as the tendency.

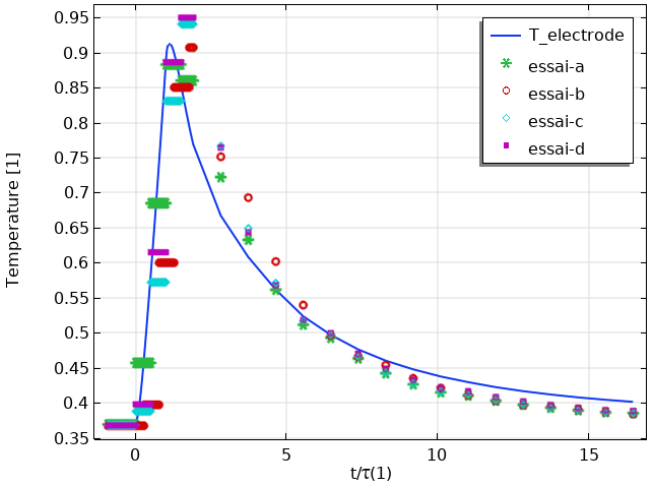

Figure 8 : Temperature of a point located in the electrode. Simulation result in blue line; experimental results in markers.

The Figure 9 shows the non-dimensional difference of electrical potential (DoP) between a point located in the electrode holder and a point located in the cooling bar. The numerical result is plotted in blue and experimental ones are represented with markers. This DoP reveals the overall power generated in the process.

Despite the significant dispersion on the experimental measurements due to the strong magnetic field created around the measurement tools, very good agreement in terms of order of magnitude is obtained.

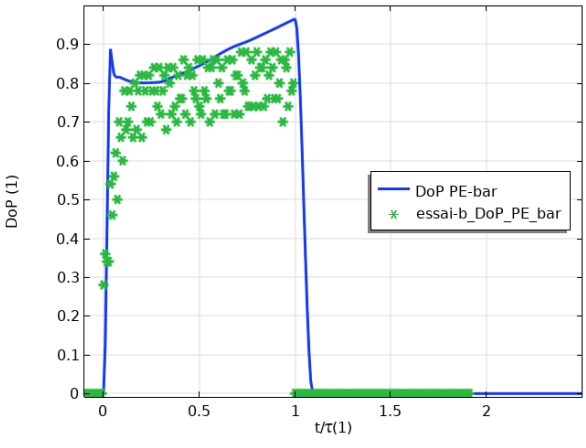

Figure 9: Difference of electrical potential (DoP) between the electrode holder and the cooling bar. Simulation result in blue line; experimental results in markers.

Finally, we compare both approaches of CR evaluation. The first one is the Mikic model and the second one is obtained by experimental measurements. Figure 10 shows the DoP between the electrode and the tip with those two approaches and compares them to DoP measurements. As we can see, experimental CR leads to an overvalued DoP where the Mikic model allows to better evaluate it even if the tendency does not follow precisely the experimental DoP.

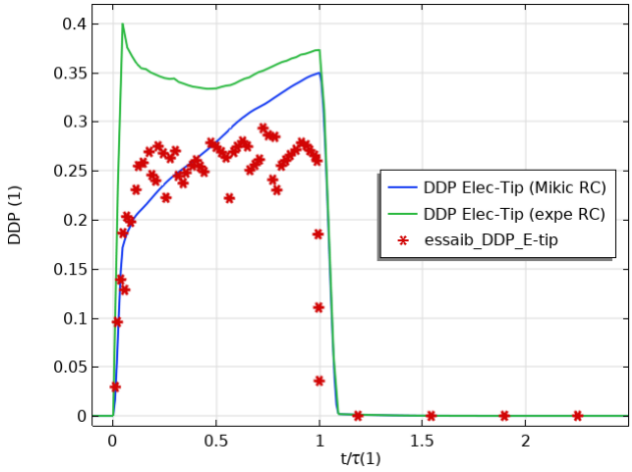

Figure 10: Comparison between Mikic model and experimental CR

Conclusion

We developed here a 3D Multiphysics model that fully represent the industrial process of resistance sintering for real contacts used in SCHNEIDER ELECTRIC breakers. Thanks to good knowledge of material properties and appropriate contact resistances estimation, the accuracy of the numerical model is remarkable. Thus, the model is a predictive tool that can be used to achieve better product quality.

A simulation application has also been developed to provide welding expert a tool of decision to achieve the Indus 4.0 goals. As the sintering aspect is now mastered, next step is the modeling of the assembly aspect to complete the hole digitalization of the sintering-assembly process.

References

1 : J.L. Wintz, S. Hardy, (2013), *Design guideline of contactors: Optimal use of assembled contacts,* Holm Conference on Electrical Contacts (HOLM), IEEE 59th, p 1-6. https://doi.org /10.1109/HOLM.2014.7031014

2 : S. R. Oke, O. O. Ige1, O. E. Falodun, A. M. Okoro, M. R. Mphahlele, P. A. Olubambi, (2019*), Powder metallurgy of stainless steels and composites: a review of mechanical alloying and spark plasma sintering,* International Journal of Advanced Manufacturing Technology, https://doi.org/10.1007/s00170-019-03400-2

3 : G. Li, H. Cui, J. Chen, X. Fang, W. Feng, J. Liu, (2017*), Formation and effects of CuO nanoparticles on Ag/SnO2,* J. Alloy Compd 696, 1228-1234. https://doi.org/10.1016/j.jallcom.2016.12.092

4 : C. Manière, U. Kus, L. Durand, R. Mainguy, J. Huez, D. Delagnes, C. Estournès, (2016), *Identification of the Norton-Green Compaction Model for the Prediction of the Ti–6Al–4V Densification During the Spark Plasma Sintering Process,* Advanced Engineering Materials, Vol 18, Issue 10, p 1720-1727.
https://doi.org/10.1002/adem.201600348

5 : B. Mikic, (1974), *Thermal contact resistance; Theoretical considerations,* Department of Mechanical Engineering, Massachusetts Institute of Technology, Int J. Heat Mass Transfer. Vol. 17, pp. 205-214.

6 : S. Bourdon, V. Bruyère, P. Rogeon, P. Namy, C. Durand, S.Roure, *Numerical Simulation Of Electro-Thermo-Mechanical Phenomena During Resistance Sintering,* Comsol Conference 2020.

7 : J. Amovin-assagba, V. Bruyère, P. Namy, C. Durand, S.Roure*; Contact Resistance Influence in Numerical Simulation of Resistance Sintering,* 19th International Multidisciplinary Modeling & Simulation Multiconference 2022

8 : R. SAIM, S. ABBOUDI, B. BENYOUCEF, A. AZZI (2007); *Analyse numérique de la convection forcée turbulente dans les tubes munis des chicanes transversales* ; 13èmes Journées Internationales de Thermique, 2007, Albi-France